Journal of Inflammation Research

Dovepress
Taylor & Francis Group

Open Access Full Text Article

ORIGINAL RESEARCH

FGF7–FGFR2 Signaling Enhances Contractile Activation of CAFs in Ovarian Cancer: Integrative Single-Cell and Spatial Transcriptomics

Songwei Feng[1,*], Zhaoyan Ding[2,*], Yuru Wang[1], Zihan Zhu[2], Wen Zhong[2], Ke Zhang[3], Yueming Zhang[1], Li Chen[1], Yun Ma[4]

[1]Department of Obstetrics and Gynaecology, The Fourth Affiliated Hospital of Soochow University, Suzhou, People's Republic of China; [2]Suzhou Medical College, Soochow University, Suzhou, People's Republic of China; [3]Department of Obstetrics and Gynaecology, Zhongda Hospital, School of Medicine, Southeast University, Nanjing, People's Republic of China; [4]Department of Obstetrics and Gynaecology, The Second Affiliated Hospital of Soochow University, Suzhou, People's Republic of China

*These authors contributed equally to this work

Correspondence: Li Chen; Yun Ma, Email soochowchenli@163.com; soochowmayun@163.com

Background: Cancer-associated fibroblasts (CAFs) are a major stromal component of high-grade serous ovarian carcinoma (HGSOC), yet their functional programs and spatial organization remain incompletely defined and inconsistently reported across studies.

Methods: We analyzed single-cell RNA-seq data from 7 treatment-naïve HGSOC tumors and integrated these findings with spatial transcriptomics from 4 HGSOC specimens. CAFs were re-clustered into functional programs, trajectories were inferred, and cell–cell communication was modeled. CAF states were mapped onto tissue sections using deconvolution and single-cell spatial mapping. Primary HGSOC CAFs and TGF-β–activated MRC5 fibroblasts (MRC5-CAFs) were used for collagen gel contraction and Western blot validation with perturbation of FGF7/FGFR2 signaling.

Results: We identified three CAF programs: matrix-associated CAFs (mCAFs), metabolic-associated CAFs (meCAFs), and proliferative CAFs (pCAFs). Trajectory analyses suggested a continuum from pCAF to mCAF to meCAF. Communication analyses highlighted an FGF7–FGFR2 axis enriched in mCAFs. Spatial analyses indicated CAF-enriched regions were spatially segregated from immune-enriched regions. In vitro, recombinant FGF7 increased AKT phosphorylation and enhanced CAF contractile activation, whereas FGF7 neutralization or FGFR2 inhibition reduced AKT phosphorylation and contractility.

Conclusion: Integrative single-cell, spatial, and functional analyses implicate an FGF7–FGFR2–PI3K/AKT axis in maintaining the contractile activation of CAFs in ovarian cancer, providing a rationale for targeting CAF signaling and ECM remodeling.

Keywords: ovarian cancer, cancer-associated fibroblasts, FGF7, extracellular matrix, single-cell transcriptomics, spatial transcriptomics

Introduction

The rapid development of omics technologies has significantly advanced the frontiers of biomedical research. Technologies such as single-cell RNA sequencing, spatial transcriptomics, and ATAC sequencing have been widely applied to study cellular heterogeneity and communication within the tumor microenvironment (TME).[1–3] These applications provide new perspectives for understanding the complexity of the tumor microenvironment and offer novel tools for exploring the functionalities of cancer-associated fibroblasts (CAFs) in ovarian cancer (OC).

Current basic research has clearly identified the origins of CAFs, suggesting they may arise from normal fibroblasts, bone marrow mesenchymal stem cells, epithelial cells, endothelial cells, or adipocytes.[4] CAFs in OC are traditionally classified based on the expression of α-SMA, a marker of smooth muscle cells.[4,5] Furthermore, Givel et al by analyzing the expression of FAP, α-SMA, CD29, PDGFRβ, FSP1, and caveolin 1 in OC, identified four CAF subtypes, where CAF-S2 and CAF-S3

https://doi.org/10.2147/JIR.S571158
Received: 10 October 2025
Accepted: 5 April 2026
Published: 21 April 2026

resemble normal fibroblasts (NFs), and CAF-S1 and CAF-S4 are primarily located at cancer and metastatic sites.[6] Galbo et al identified six genetic subtypes of CAFs, including myofibroblastic, fibroblastic, two inflammatory types, normal, and proliferative CAFs.[7] Luo et al categorized CAFs in pan-cancer into three main states, highlighting their distinct interactions with other cellular components, which are closely linked to the prognosis of immunotherapy.[8] Ma et al defined four main CAF subtypes in solid tumors—iCAF, mCAF, meCAF, and pCAF—pointing out that the proportions of CAF subtypes vary across different cancer types.[9] These studies indicate that the classification of CAFs remains highly controversial, especially among Chinese population samples.

In fact, one of the challenges faced by the scientific community is achieving consensus on the classification and nomenclature of CAFs. Due to the inconsistency in classifying and naming CAFs, we will discuss their functions from a broader perspective that focuses on the functional and developmental characteristics of CAFs, rather than specific subtype names or markers. Our study uses seven single-cell samples combined with the latest bioinformatics algorithms to re-annotate and explore the heterogeneity of CAF subtypes. This analysis reveals developmental processes and cellular communication, highlighting key interactions involving FGF7.

Materials and Methods

Data Source

Bulk transcriptome datasets used for validation included a microdissected stromal dataset (GSE40595), RNA-seq of MRC5 and TGF-β–activated MRC5-CAFs (GSE97829), and TCGA-OV for survival analysis. Public single-cell RNA sequencing (scRNA-seq) data were obtained from the GEO database (GSE184880), generated from fresh surgical specimens of HGSOC and normal ovarian tissues using the 10x Genomics Chromium Single Cell 3′ v3.1 platform and processed with Cell Ranger (v3.1.0). We analyzed 7 treatment-naïve HGSOC tumors. FIGO stage information from GEO annotations was used to categorize tumors as early stage (FIGO I–II, n=3) or advanced stage (FIGO III–IV, n=4). Spatial transcriptomics (ST) data were obtained from a published HGSOC cohort from the MD Anderson Cancer Center, available via CodeOcean/figshare, including 4 10x Genomics Visium slides (A4, A5: early stage; A10, A12: advanced stage). The scRNA-seq and ST cohorts represent different patients and were analyzed separately; integration was used only for reference-based deconvolution and spatial mapping.

Quality Control

Single-cell data underwent quality control, including gene detection ranging from 200 to 12,000 genes per cell, mitochondrial gene content below 40%, and total detected molecules between 200 to 60,000. After quality control, 32,043 cells and 21,785 genes were included for bioinformatics analysis. Post-quality control, the CellCycleScoring function was used for cell cycle scoring; NormalizeData and ScaleData functions for data normalization and highly variable gene selection, with the top 2000 fluctuating genes identified, mitigating S and G2M phase scores. The RunHarmony function integrated samples and mitigated batch effects. Principal Component Analysis (PCA) and the ElbowPlot function visualized the variance trend of components, selecting the top 30 components for downstream analysis. FindNeighbors and FindClusters functions clustered cells, visualized using t-SNE. ST data were normalized using SCTransform and integrated across slides using Harmony. Differentially expressed genes were identified with FindAllMarkers (min.pct=0.10, logfc.threshold=0.25).

Cell Culture

No established cell lines specifically for OC-associated CAFs have been reported. Existing research has only succeeded in creating immortalized human CAFs cell lines for cancers such as breast, colon, and pancreatic cancer.[10] Therefore, similar to previous experimental studies on CAFs from OC, our CAFs were derived from patients pathologically diagnosed with HGSOC. The extraction of CAFs was based on our previous research protocols.[11] Human embryonic lung fibroblasts (MRC5), authenticated via STR cell identification and long-term preserved in our research group, were cultured. Cells were cultured in DMEM/F-12 medium at 37°C and 5% CO2, supplemented with 1% penicillin/streptomycin and 10% fetal bovine serum. After one week of induction with

TGF-β1 (50ng/mL), MRC5 cells transitioned into an activated phenotype,[11] MRC5-CAFs. hFGF7 was added to the medium at concentrations of 10 ng/mL and 20 ng/mL for 48 hours.[12] According to references,[13] cells were treated with 5 μM/mL of AZD4547, a highly sensitive pan-FGFR inhibitor, for 48 hours. In neutralization experiments, a pre-treatment with 1 μg/mL of FGF7 neutralizing antibody was applied to the culture medium for 4 hours.[12]

Collagen Contraction

The contractility of MRC5-CAFs and primary CAFs was evaluated using a floating collagen matrix model. A mixture containing 6×10^4 cells in type I rat tail collagen (168.75 μL DMEM/F-12 medium, 31.25 μL collagen, 0.72 μL 1N NaOH) was added to each well of a 96-well ultra-low attachment plate. After 24 hours of incubation, images were captured.

Western Blotting

Western blot analysis was performed following established standard protocols. The procedure employed primary antibodies targeting beta-Actin (20536-1-AP), α-SMA (14395-1-AP), AKT (10176-2-AP), and phosphorylated AKT (p-AKT) (80455-1-RR), all sourced from Proteintech, China. Horseradish peroxidase-conjugated goat anti-mouse and anti-rabbit antibodies (Proteintech, China) served as secondary antibodies. Detection was achieved through enhanced chemiluminescence (ECL) (P10300, NCM, China), facilitating the visualization of protein bands.

FGF7 Correlation Analysis

The ESTIMATE algorithm was applied to bulk transcriptome datasets to evaluate the relationship between stromal scores and normalized FGF7 expression. In the microdissected OC stromal dataset (GSE40595), correlation between ACTA2 (α-SMA) and FGF7 was assessed in tumor stroma samples. For MRC5 and TGF-β–treated MRC5-CAFs (GSE97829), differential expression was analyzed using limma ($|logFC|>2$, adjusted $p<0.05$).

Cell Annotation

Cells were preliminarily annotated using classical cell marker genes reported in references,[14,15] providing a reliable basis for identifying primary cell types, including epithelial (EPCAM, KRT18, KRT19, CDH1), fibroblasts (DCN, THY1, COL1A1, COL1A2), endothelial (PECAM1, CLDN5, FLT1, RAMP2), T cells (CD3D, CD3E, CD3G, TRAC), NK cells (NKG7, GNLY, NCAM1, KLRD1), and B/plasma cells (CD79A, IGHM, IGHG3, IGHA2). To enhance annotation accuracy, expression similarities between subgroups were calculated using the AverageExpression and cor functions, constructing a global clustering similarity matrix. Cell subgroup accuracy was validated by comparing marker-based annotations with unsupervised clustering similarity matrix outcomes.

The Conditional Autoregressive-based Deconvolution (CARD) algorithm was applied to spatial transcriptomics,[16] segmenting spatial regions into tumor, non-tumor, and different cell types, with spatial mapping performed using CARD_SCMapping function.

CAFs Re-Annotation

All CAFs were selected using the subset function, with the top 30 dimensions adjusted by the harmony algorithm, and dimensionality reduction via the RunTSNE function. FindNeighbors and FindClusters segregated CAFs into subgroups, identifying differential expression genes for each cluster using FindAllMarkers, focusing on upregulated genes expressed in at least 10% of cells, with a log fold change threshold of 0.25. GO enrichment analysis post-differential analysis identified biological processes (BPs) engaged by CAF subgroups, grouping BPs-consistent subgroups as identical CAF clusters. Functional verification of different CAF subgroups utilized the msigdbr package to retrieve GO and Hallmark gene sets from the Molecular Signatures Database, extracting gene lists associated with muscle contraction, cell cycle, extracellular matrix organization, collagen biosynthesis, angiogenesis, and inflammatory response pathways. The AddModuleScore function calculated gene set scores within cells.

Malignant Cell Identification

The inferCNV algorithm, designed for analyzing copy number variation (CNV) events in single-cell sequencing data, analyzed epithelial cell populations in single-cell and spatial transcriptomics datasets for CNV detection and malignancy inference. Genes were arranged according to chromosomal positions, with CNVs estimated by averaging CNVs of each gene and its adjacent 100 genes (50 on each side). Cell CNV scores were calculated by squaring and summing all gene CNVs within a cell. inferCNV analysis employed a 0.1 cutoff, with clustering and denoising options activated.

Single-Cell Regulatory Network Inference and Clustering

Single-cell regulatory network inference and clustering (SCENIC)[17] inferred gene co-expression regulatory networks using GENIE3 and GRNBoost algorithms, based on expression data patterns and correlations, identifying potential gene-gene interactions. RcisTarget identified regulatory factors' binding motifs, revealing direct target Regulons within the gene network. AUCell algorithm scored each cell's Regulon activity, producing a binary matrix predicting cell activity, reflected in Regulon activity levels across different cell states. Heatmaps displayed transcription factor activity score differences across CAF subgroups using pheatmap, with relative ranking scores (RRS) for each transcription factor calculated using calculate_rrs and visualized with plot_rrs_ranking function.

Metabolic Analysis

Single-Cell Pathway Analysis (SCPA)[18] and scMetabolism algorithms[19] conducted metabolic pathway analysis on various CAF subgroups. Expression matrices for each CAF subgroup underwent SCPA and scMetabolism analysis, with compare_pathways function comparing metabolic pathway activities between cell groups, visualized using volcano plots and heatmaps for module scores across metabolic pathways.

Pseudotime Analysis

Pseudotime analysis, reconstructing cellular changes over time, employed Monocle2 and Slingshot algorithms to reveal the dynamic differentiation process of CAFs.[20] Monocle objects were converted to CellDataSet format, with cell trajectories analyzed using Monocle's features. Size factors and dispersions were estimated, selecting genes for ordering based on expression and dispersion criteria, excluding specific genes to minimize technical variability. Dimensionality reduction used DDRTree, with cells ordered by orderCells to reveal potential developmental or differentiation trajectories. Branch Expression Analysis Modeling (BEAM) function analyzed branching points in CAF differentiation, identifying genes with significant expression changes at branch points, visualized using heatmaps. Slingshot inferred differentiation trajectories, inputting tsne-dimensionally reduced CAF subgroup Seurat objects, with RunSlingshot establishing differentiation paths.

GeneSwitches

GeneSwitches analyzed significant expression pattern changes in genes and related pathways during CAF differentiation.[21] Data conversion from Monocle cds to binary expression using convert_monocle2 and binarize_exp functions preceded down-sampling via find_switch_logistic_fastglm for switch gene selection. filter_switchgenes filtered genes with an r^2 threshold of 0.1, with significant pathways identified using find_switch_pathway and hypergeometric tests (sig_FDR=0.05). merge_pathways merged upregulated pathways during development based on similarity (ratio = 0.8). plot_pathway_density visualized density plots in chronological order.

Survival Analysis

CAF state signatures were defined by differential expression in Monocle-inferred CAF states. Single-sample gene set enrichment analysis (ssGSEA) scores were computed for each TCGA-OV tumor using the IOBR package. Patients were stratified into high versus low score groups using the median score as the primary cutoff; an optimal cutpoint (surv_cutpoint) was used as a sensitivity analysis. As a control, we also computed an overall CAF abundance score (based on pan-CAF markers) and included it as a covariate in multivariable Cox models to assess whether state-specific

signatures provided information beyond global CAF content. Survival differences were assessed using Kaplan–Meier curves with Log rank tests and Cox proportional hazards models. Proportional hazards assumptions were evaluated using Schoenfeld residuals; when assumptions were not met, restricted mean survival time (RMST) analyses were used as a robustness check.

Cell Communication Analysis

The CellChat package analyzed and visualized cell-cell communication networks in single-cell sequencing data,[22] setting secretory signals from the CellChatDB.use database for communication analysis. identifyOverExpressedGenes and identifyOverExpressedInteractions identified overexpressed secretory signal-related genes and interactions in cell groups. computeCommunProb calculated cell communication probabilities, with filterCommunication selecting supported communication events. computeCommunProbPathway and aggregateNet calculated communication pathway probabilities and aggregated networks, constructing an integrated communication network model. Various visualization methods displayed cell communication network differences and characteristics, including netVisual_diffInteraction for differential interaction networks, netAnalysis_signalingRole_scatter for two-dimensional signaling intensity plots, and netVisual_bubble for bubble charts showcasing cell communication patterns with different CAF states as outputs.

CellTrek

Spatial transcriptomics, while adept at spatially mapping gene expression on tissue sections, is limited to measuring gene expression in small areas within a mixture of cells and cannot provide single-cell resolution. To address this, we utilized the CARD algorithm for deconvolution of mixed regions to estimate the proportions and classifications of different cell types. However, most deconvolution methods only yield categorical labels and lack the ability to infer continuous and more detailed cellular information at a spatial resolution. To overcome this limitation, we introduced the CellTrek algorithm, which allows for the direct mapping of CAFs clusters back to their spatial coordinates on tissue sections. CellTrek enables the identification and localization of these cell populations while preserving spatial information, particularly suitable for smaller and more precisely defined cell groups. The run_kdist function calculates the average distance k of different cell types relative to CAFs subgroups to assess their spatial distribution differences, sorted using RAA. The celltrek_chart function generates a chart of cell locations, optimizing the mapping of cell positions to prevent overlap and ensure accuracy of spatial information using the repel_r and repel_iter parameters. Finally, pheatmap visualizes the spatial distribution differences of various cell types across tumor stages.

Statistical Analysis

Statistical analyses were conducted in R Studio to assess the significance of observed differences and correlations in bioinformatics analyses. The independent samples *t*-test was used to compare quantitative data between two groups, while analysis of variance (ANOVA) was applied when data involved three or more groups. Pearson correlation analysis was employed to explore the relationships between variables. Differences were considered statistically significant at a p-value of less than 0.05.

Results

Heterogeneity of Single Cell Data

Quality control was conducted on single-cell sequencing data, identifying 21 clusters (Figure 1A). A bubble chart displayed the expression of marker genes within these clusters (Figure 1B): clusters 0, 8, and 15 highly expressed epithelial markers; clusters 7, 18, and 19 highly expressed CAFs markers; Cluster 13 highly expressed endothelial markers; clusters 4, 10, 1, 5, and 6 highly expressed T cell markers; Subgroup 2 highly expressed NK cell markers; and clusters 11, 14, 17, and 20 highly expressed B/plasma cell markers; clusters 9, 16, 3, and 12 highly expressed myeloid cell markers. An unsupervised clustering matrix heatmap (Figure 1C) demonstrated that clusters 0, 8, and 15; clusters 7, 18, and 19; clusters 2, 4, 10, 1, 5, and 6; clusters 11, 14, 17, and 20; clusters 9, 16, 3, and 12; and cluster 13 were accurately classified into corresponding meta-clusters, validating the annotation results. Ultimately, a total of 32,043 cells were categorized into seven cell types (Figure 1D and E): T cells ($CD3D^+$), myeloid cells (LYZ^+), NK cells ($NKG7^+$),

 https://doi.org/10.2147/JIR.S571158

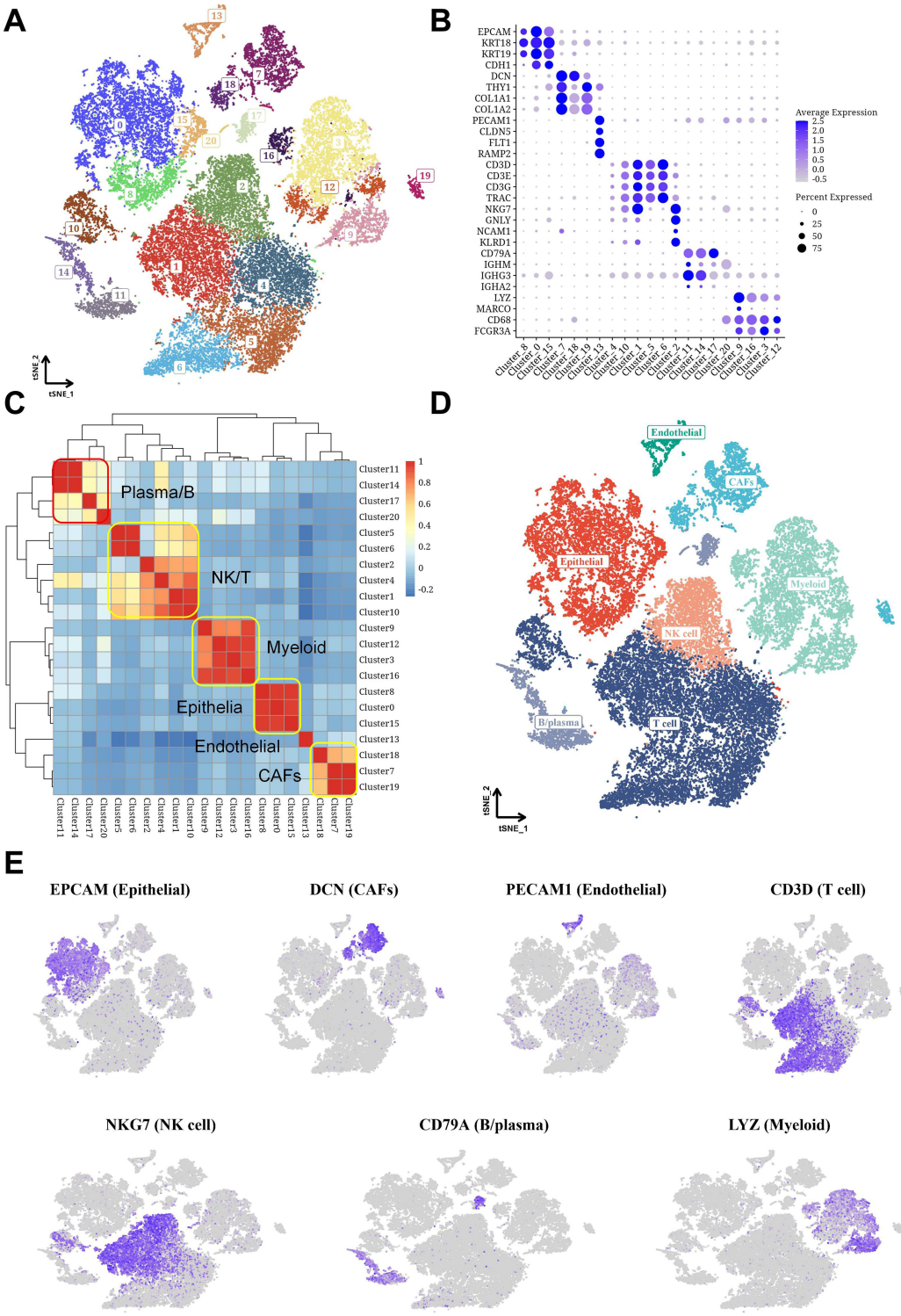

Figure 1 Heterogeneity of single-cell data in ovarian cancer. (**A**) t-SNE plot showing the clustering of 21 distinct cell clusters based on single-cell RNA sequencing data. Each cluster is color-coded and labeled with its respective cluster number. (**B**) Bubble plot displaying the expression levels of marker genes within the identified clusters. The size and color intensity of the bubbles represent the expression level of specific marker genes in each cluster. (**C**) Heatmap showing the unsupervised clustering matrix, validating the classification of clusters into major cell types. The dendrogram on the left indicates the hierarchical clustering of the cell types. (**D**) t-SNE plot illustrating the classification of cells into seven major cell types: T cells (CD3D+), myeloid cells (LYZ+), NK cells (NKG7+), endothelial cells (PECAM1+), epithelial cells (EPCAM+), plasma/B cells (CD79A+), and CAFs (DCN+). Each cell type is color-coded and labeled accordingly. (**E**) Feature plots showing the expression of key marker genes across the t-SNE map: EPCAM (epithelial cells), DCN (CAFs), PECAM1 (endothelial cells), CD3D (T cells), NKG7 (NK cells), CD79A (B/plasma cells), and LYZ (myeloid cells). The intensity of the color represents the expression level of each marker gene in the cells.

https://doi.org/10.2147/JIR.S571158

endothelial cells (PECAM1$^+$), epithelial cells (EPCAM$^+$), plasma/B cells (collectively referred to as B cells) (CD79A$^+$), and CAFs (DCN$^+$).

Gene expression within cells was organized according to chromosomes 1 through 22, and a heatmap displayed the CNV scores of epithelial cells referenced to normal cells (B cells) (Figure S1A). A t-SNE plot visualized the distribution of CNV (Figure S1B). To further explore the proportions of each cell subgroup in different samples, a bar chart was created (Figure S1C). In advanced-stage samples, Sample 3 predominantly contained T cells (64.53%); Sample 4 primarily consisted of epithelial cells (41.06%); Sample 7 had a significant proportion of T cells (50.75%). In early-stage samples, Sample 1 was mainly composed of myeloid cells (28.94%), followed by T cells (25.81%); Sample 2 was predominantly epithelial cells (32.58%); Sample 5 mostly contained T cells (60.57%); Sample 6 had comparable proportions of CAFs and epithelial cells, 36.83% and 34.70%, respectively, indicating significant heterogeneity across different samples. Subsequently, a bar chart again highlighted the distribution differences of various cell clusters between early and advanced-stage patients (Figure S1D). Overall, T cells were the most abundant cell type (11,779 cells), endothelial cells were the scarcest (602 cells), and epithelial cells exhibited the highest transcript and CNV levels, consistent with their highly malignant nature, prompting a revision of the cell annotation from Epithelial to Neoplastic. Compared to early-stage patients, advanced-stage patients showed a significant increase in proportions of CAFs (6.32% to 93.68%), endothelial cells (5.64% to 94.36%), tumor epithelial cells (31.14% to 68.86%), NK cells (32.11% to 67.89%), and myeloid cells (23.99% to 76.01%); however, the proportion of B/plasma cells significantly decreased (54.78% to 45.22%), and T cells showed little change (49.41% to 50.59%).

Thus, OC exhibits significant heterogeneity, which cannot solely be assessed through changes in cell proportions for immune characterization.

Heterogeneity of Spatial Transcriptome Data

Bar charts displayed the quality control results for the nFeature_RNA and nCount_RNA parameters (Figure S2A), indicating high sequencing quality across various spots. Additionally, a heatmap matching spatial location information with transcriptomic data showed richer sequencing outcomes concentrated in the tumor areas. The CARD algorithm was used to classify spots into tumor and non-tumor areas. Within the tumor regions, four clusters were identified. A heatmap revealed cluster 0 with key markers such as MUC5B and CLU, cluster 1 with LHX1 and PCK1, cluster 2 with IL1RAP and CLDN6, and cluster 3 with RNU4ATAC (Figure S2B). In early-stage patients, A4 predominantly exhibited cluster 0, whereas A5 was mainly composed of cluster 3. In advanced-stage patients, A10 was dominated by cluster 1, and A12 by cluster 2 (Figure S2C). These results indicate high heterogeneity within the tumor areas of the samples. In the non-tumor areas, a heatmap showed cluster 0 characterized by markers like CLU and BCYRN1, cluster 1 by SPP1 and LDHA, cluster 2 by ADH1B and CD36, and cluster 3 by RPL13AP3 and RPL13AP6 (Figure S2D). Early-stage patients A4 and A5 predominantly featured cluster 0, while advanced-stage patients A10 and A12 were mainly characterized by cluster 1 (Figure S2E). These findings suggest lower heterogeneity in the non-tumor areas of the samples. A t-SNE plot then visualized the distribution of clusters across all areas, combining the four samples (Figure S2F).

Further deconvolution analysis using the CARD algorithm determined the detailed cell types and proportions. A heatmap displayed the distribution of cells across different samples (Figure 2A), revealing that immune cells such as T cells, B cells, and NK cells were primarily located in non-tumor areas, while the presence of immune cells was notably reduced in tumor areas, with CAFs encircling them like a barrier. In spatial transcriptomics data, advanced-stage patients compared to early-stage ones showed an increased proportion of immune cells and a decreased proportion of stromal cells (CAFs and endothelial cells), likely due to a higher density of tumor cells and differences in the sequenced areas (Figure 2B). Finally, combining spatial location and cell annotation information, the general conditions of each sample were comprehensively presented (Figure 2C).

Together, these spatial analyses support a model in which CAF-rich regions and immune-rich regions are spatially segregated in HGSOC tissues. We interpret this as evidence of compartmentalization rather than direct proof of a physical barrier, which will require further validation.

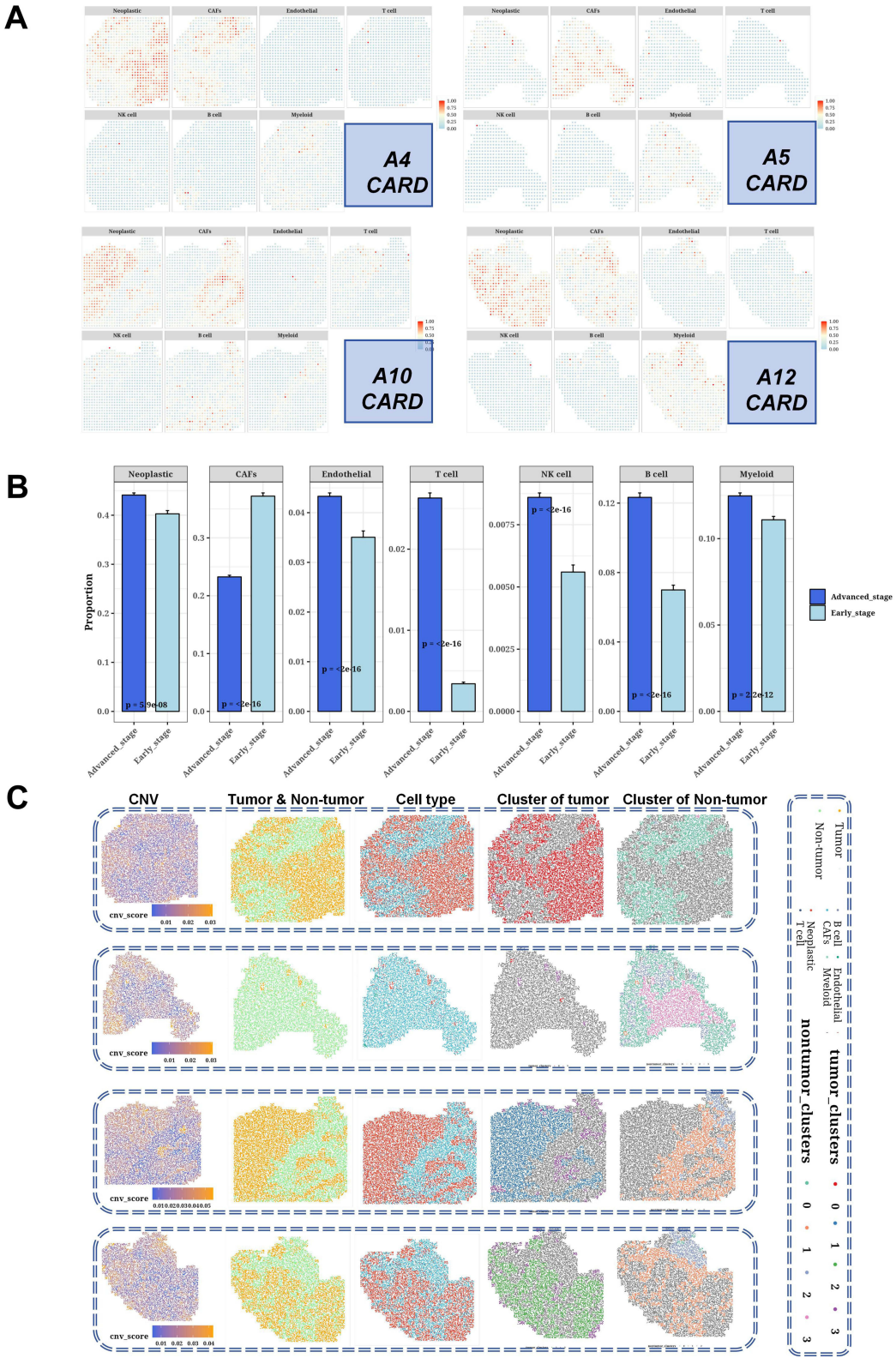

Figure 2 Spatial distribution characteristics of CAFs in ovarian cancer. (**A**) CARD-based deconvolution maps showing the estimated proportion (0–1) of each major cell type across spots in early-stage samples (A4, A5) and advanced-stage samples (A10, A12). (**B**) Bar plots comparing cell-type composition between early and advanced-stage samples, computed at the sample level. Bars show mean values and dots indicate individual samples. Error bars indicate SD. (**C**) t-SNE plots visualizing the clustering of tumor and non-tumor spots and their inferred cell-type composition. Tumor versus non-tumor designation follows CARD-inferred neoplastic content and tumor marker expression (see Methods).

 https://doi.org/10.2147/JIR.S571158

Reannotation of CAFs in Ovarian Cancer

By applying further clustering, we identified ten cellular clusters (Figure 3A). We then filtered out statistically significant genes for enrichment analysis and studied their involvement in biological processes. The enrichment analysis revealed that clusters 0, 1, 3, and 6 are primarily related to extracellular matrix organization, representing the mCAF (Figure 3B–E); clusters 2 and 9 are associated with responses to oxygen levels and hypoxia, representing the meCAF (Figure S3A); cluster 4 is involved in a range of ribosomal-related biological processes necessary for ribosomes to support new protein synthesis during cell division and proliferation, representing the pCAF; cluster 5 is related to actin filament-based processes where the cytoskeletal system, including actin filaments, drives cytoplasmic division through mechanisms of contraction and disassembly, thus facilitating the completion of cell division, therefore, representing the pCAF; clusters 7 and 8 are involved in similar functions, including ribonucleoprotein complex biogenesis and DNA/RNA replication and modification during cell division, representing the pCAF (Figure S3B). Finally, a t-SNE plot once again displayed the distribution of mCAF, meCAF, and pCAF subtypes (Figure 3F).

Functional Heterogeneity of CAFs in Ovarian Cancer

In OC, three CAF clusters were identified: mCAF, meCAF, and pCAF. However, these do not include the iCAF found in pan-cancer CAF analyses. Thus, we hypothesize that there might be heterogeneity among CAF clusters across different cancers, and a cluster in mCAF, meCAF, and pCAF may perform functions similar to those of iCAFs.

Further investigation into the functional heterogeneity of these three CAF clusters was conducted, using heatmaps to display differences in enriched pathways among the CAF clusters (Figure 4A). Results indicate that meCAF is associated with hypoxia and classical glycolytic responses, akin to the metabolic CAFs reported in pancreatic ductal adenocarcinoma.[23] pCAF significantly correlates with the cell cycle and contractility, consistent with findings from a previous study on proliferative CAFs in pan-cancer analyses.[9] In addition to its association with ECM functions, mCAF is also highly related to inflammatory responses, aligning with findings from studies on stromal CAFs in cervical squamous cell carcinoma.[24] GO enrichment analysis was again performed for mCAF, meCAF, and pCAF, showing that mCAF is primarily linked to ECM functions (Figure 4B), meCAF to oxygen responses and cellular metabolism (Figure 4C), and pCAF to pathways related to cell proliferation (Figure 4D). Considering the metabolic characteristics of meCAF, the SCPA algorithm was used to study their metabolic pathway activities. As expected, glycolytic and amino acid metabolism pathways were significantly enriched in meCAF (Figure 4E), suggesting that CAFs support cancer cells through glycolysis in the hypoxic tumor microenvironment, potentially leading to a reverse Warburg effect induced by meCAF. Given the metabolic abnormalities in different CAFs, the scMetabolism algorithm was utilized to explore mechanisms of metabolic reprogramming driven by CAFs. mCAF showed higher activity in glycosaminoglycan and amine-derived hormones, while fructose, triglyceride, and aspartate and asparagine were enriched in pCAF. Beyond glycolysis, pathways involved in phenylalanine and Vitamin B1 metabolism were also significantly enriched in meCAF (Figure 4F).

Transcriptional Regulation and Differentiation Trajectory of CAFs

The SCENIC algorithm identified transcriptional regulatory features of three CAF clusters. The RSS indicates the likelihood of genes being regulated by specific transcription factors, with higher RSS values denoting greater regulatory specificity. Ranking different transcription factors by RSS (Figure 5A), we found that the top four transcription factors in mCAF were FOS, FOSL2, JUN, and JUND; in pCAF, they were MEF2C, FOS, JUN, and JUND; in meCAF, they were FOSL1, CEBPB, DDIT3, and GLIS2. This suggests a relative transcriptional consistency between pCAF and mCAF (FOS, JUN, JUND), whereas significant changes in meCAF, with only the FOSL family being consistent, indicate that pCAF and mCAF are developmentally closer, while meCAF shows greater differentiation. The heatmap comparing transcription factor regulatory activity across the three CAFs (Figure 5B) shows that pCAF significantly upregulates factors like BCLAF1[25] (related to apoptosis, cell cycle regulation, and DNA damage repair), GATA4[26] (cell development and differentiation), and E2F1[27] (cell cycle regulation and DNA damage response), confirming the highly proliferative nature of pCAF. In mCAF, CREB3L1[28] (cell stress response), ZEB1[29] (a key regulator of EMT), and IRF1[30] (anti-tumor

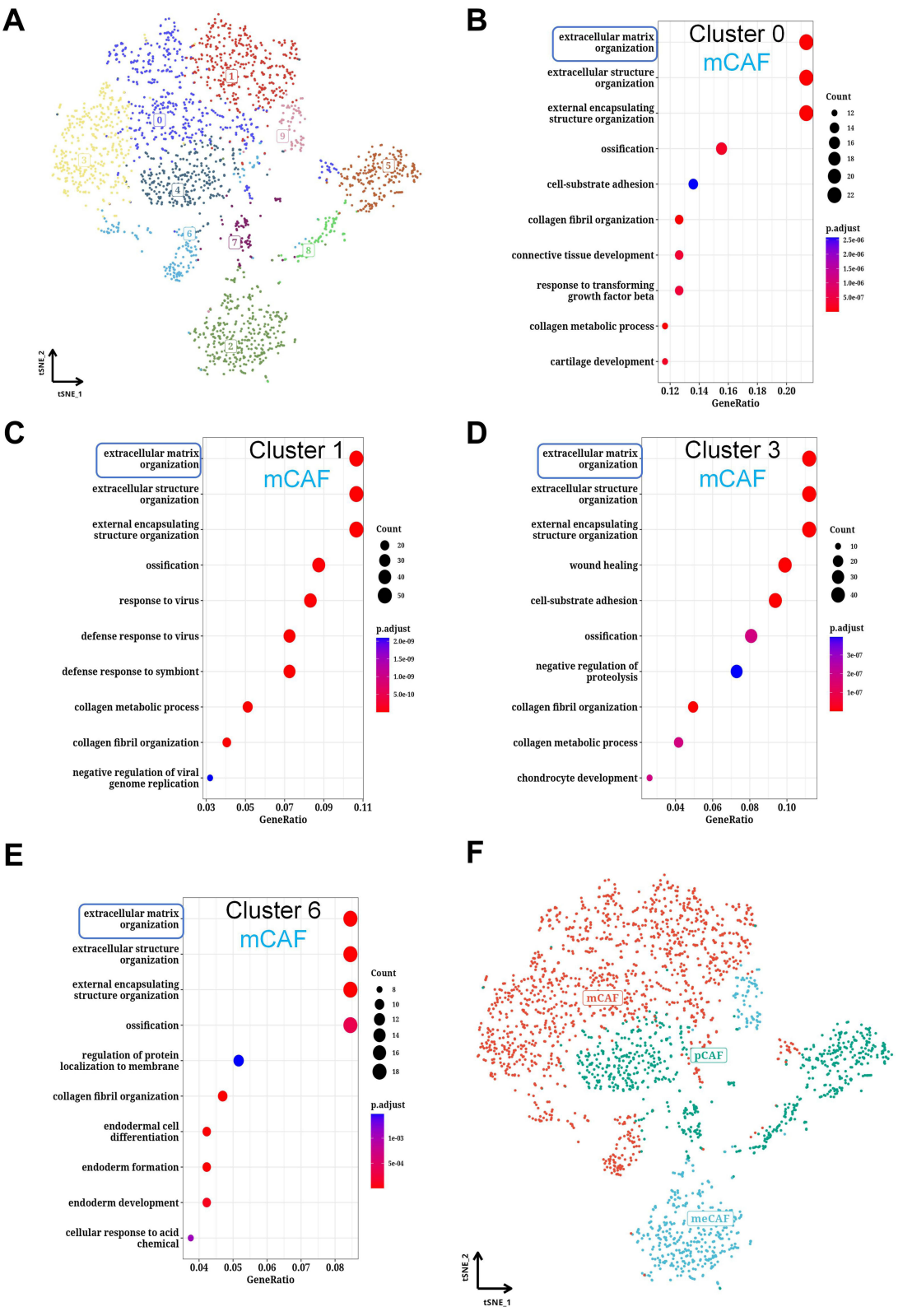

Figure 3 Reannotation of CAFs in ovarian cancer. (**A**) t-SNE plot showing the clustering of CAFs into ten distinct cellular clusters. Each cluster is color-coded and labeled with its respective cluster number. (**B**) GO enrichment analysis for Cluster 0, showing significant enrichment in extracellular matrix organization and related processes. This cluster is classified as mCAF. (**C**) GO enrichment analysis for Cluster 1, showing significant enrichment in extracellular matrix organization and related processes. This cluster is classified as mCAF. (**D**) GO enrichment analysis for Cluster 3, showing significant enrichment in extracellular matrix organization and related processes. This cluster is classified as mCAF. (**E**) GO enrichment analysis for Cluster 6, showing significant enrichment in extracellular matrix organization and related processes. This cluster is classified as mCAF. (**F**) t-SNE plot displaying the distribution of mCAF, meCAF, and pCAF subtypes among the clusters. Each subtype is color-coded, highlighting the spatial organization and differentiation states of CAFs.

https://doi.org/10.2147/JIR.S571158

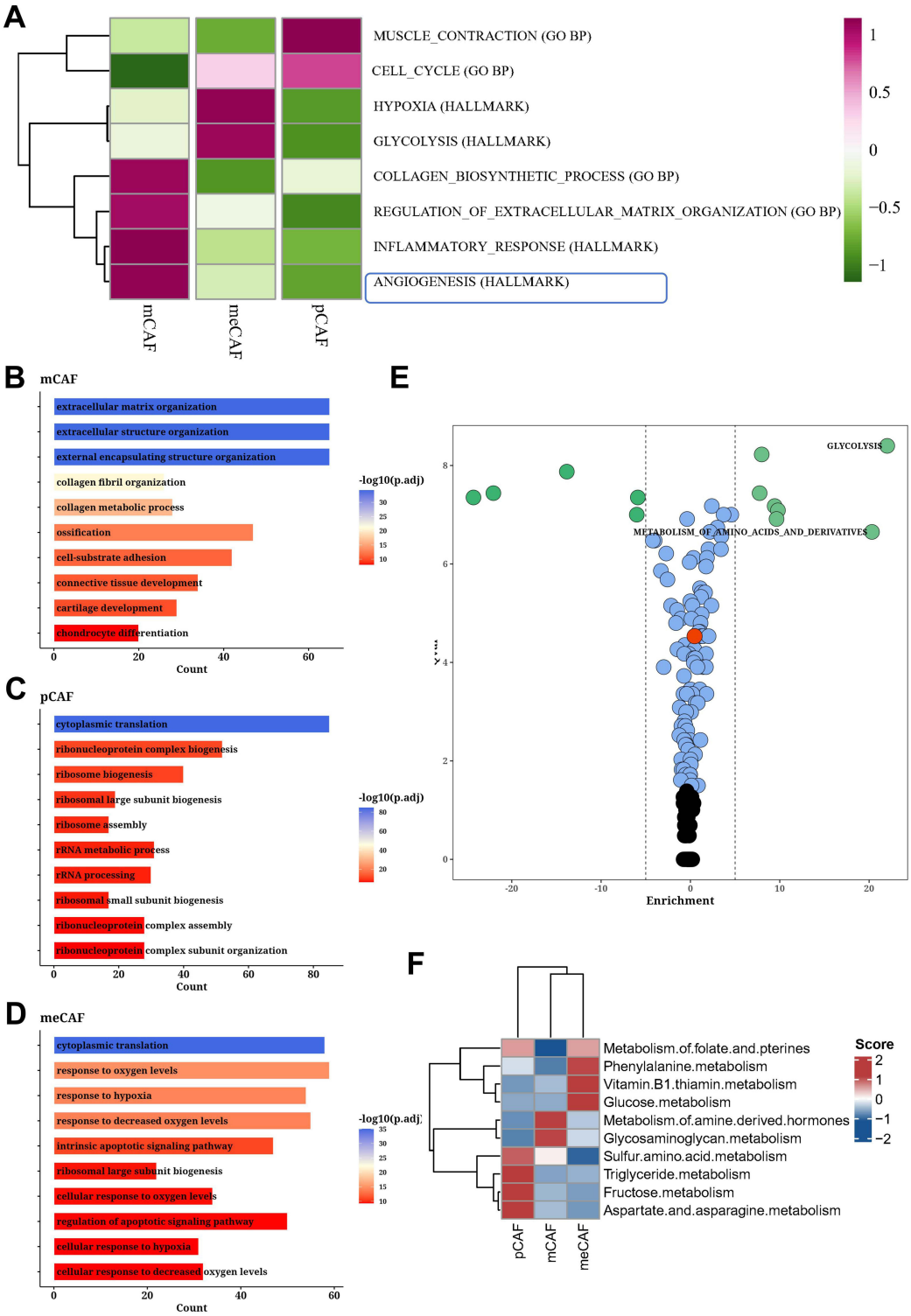

Figure 4 Functional heterogeneity of CAF subtypes in ovarian cancer. (**A**) Heatmap of hallmark gene sets showing differential pathway activity across mCAF, pCAF, and meCAF subtypes. Pathways include muscle contraction, cell cycle, hypoxia, glycolysis, collagen biosynthetic process, regulation of extracellular matrix organization, inflammatory response, and angiogenesis. (**B**) GO enrichment analysis for mCAF subtype, indicating significant enrichment in extracellular matrix organization, collagen fibril organization, ossification, cell-substrate adhesion, connective tissue development, and cartilage development. (**C**) GO enrichment analysis for pCAF subtype, showing significant enrichment in cytoplasmic translation, ribonucleoprotein complex biogenesis, ribosome biogenesis, rRNA processing, and ribosomal subunit organization. (**D**) GO enrichment analysis for meCAF subtype, highlighting significant enrichment in cytoplasmic translation, response to oxygen levels, response to hypoxia, apoptotic signaling pathway, and ribosomal subunit biogenesis. (**E**) SCPA algorithm results showing significant enrichment of glycolytic and amino acid metabolism pathways in CAF subtypes. (**F**) Heatmap showing the differential metabolic pathway activity across pCAF, mCAF, and meCAF subtypes, including folate metabolism, phenylalanine metabolism, glucose metabolism, and others.

https://doi.org/10.2147/JIR.S571158

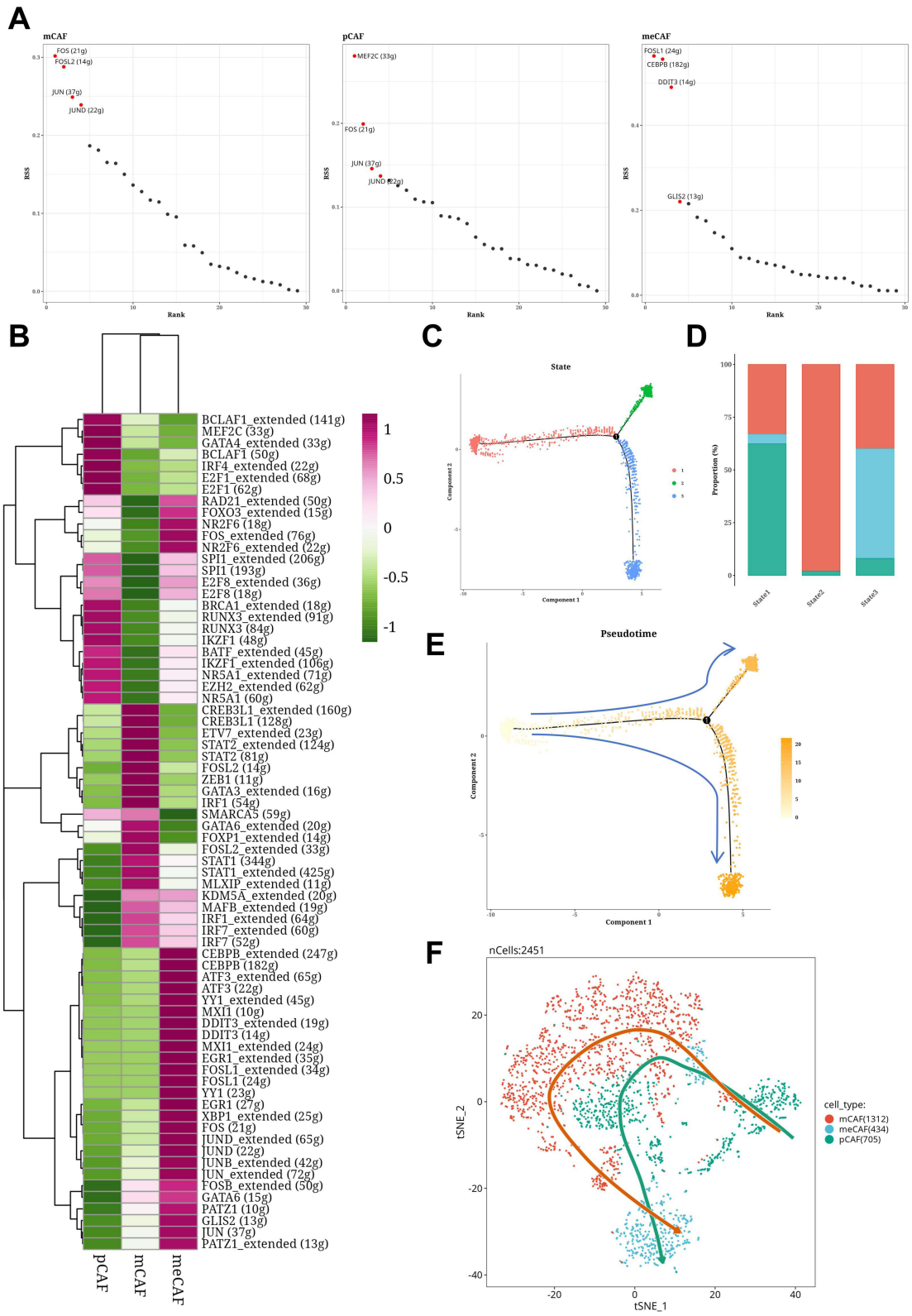

Figure 5 Transcriptional regulation and differentiation trajectory of CAFs in ovarian cancer. (**A**) Relative ranking scores (RRS) indicating the likelihood of genes being regulated by specific transcription factors in mCAF, pCAF, and meCAF subtypes. (**B**) Heatmap comparing transcription factor regulatory activity across the three CAF subtypes. Key transcription factors for each subtype are highlighted, showing distinct regulatory patterns. (**C**) Monocle algorithm results showing the ordering of single cells in a two-dimensional space based on differentiation states. Cells are colored based on their assigned state. (**D**) Bar chart displaying the proportions of CAF subtypes in different developmental states. Red indicates early states, and green indicates late states. (**E**) Pseudotime analysis illustrating the differentiation trajectory of CAFs, with arrows indicating the direction of differentiation from early to late states. (**F**) Slingshot algorithm results identifying differentiation trajectories among mCAF, pCAF, and meCAF subtypes. The lines indicate the predicted paths of differentiation.

immunity) are notably upregulated, confirming mCAF's connection to ECM shaping and inflammatory immune responses. In meCAF, ATF3[31] (cell stress), YY1[32] (a multifunctional transcription factor), XBP1[33] (cell stress), and the AP-1 complex[34] (FOS-JUND-JUNB-JUN) are significantly upregulated, confirming meCAF's multifunctionality and metabolic role.

The Monocle algorithm ordered single cells in a two-dimensional space based on two principal components, with each dot representing a cell and numbers within black circles indicating nodes where different cell states were determined during trajectory analysis (Figure 5C). CAFs exhibited three states, located on the left (state1) and right (state2/3) sides of the nodes. Labeling three types of CAFs (Figure S4A) and analyzing proportions revealed that the majority of mCAF cells were in state2; most pCAF cells were in state1; meCAF dominated state3 (Figure 5D). Pseudotime, representing the sequence of time, was annotated on cells, showing the darkest color at the lower right end and the lightest at the left end, gradually extending to the right (Figure 5E). Cells were also labeled by tumor stage, revealing that the developmental starting end mostly consisted of CAFs from early-stage patients, while both branches ended with CAFs from advanced-stage patients (Figure S4B). The Slingshot algorithm identified two developmental trajectories, both pCAF-mCAF-meCAF, consistent with the two branches found in the Monocle analysis, with the highly proliferative pCAF always at the "initial state" and the functionally diverse meCAF at the "terminal state" (Figure 5F).

Cell developmental branch points often represent fate decisions, where one lineage progresses along the original path and another diverges. To identify genes influencing fate decisions, BEAM analysis was performed to create a heatmap (Figure S4C). The heatmap's top represents conditions before and after the bifurcation, with the left side (fate1) representing state2 (dominated by mCAF) and fate2 representing state3 (dominated by meCAF). The heatmap from the center outward represents two lineages, with different clusters indicating genes that exhibit similar trends in pseudotime analysis. In the development towards state3 (dominated by meCAF), metabolic genes such as ANGPTL4[35] (related to fatty acid metabolism), SLC2A1 (glucose transport), PGK1,[36] and LDHA[37] (both glycolysis-related) showed increased expression, while cytokine-related genes CXCL10, CXCL12, and ECM-related genes COL3A1, COL1A1, and COL5A1 were downregulated. Conversely, in the development towards state2 (dominated by mCAF), genes related to ECM composition like COL3A1, COL1A1, COL5A1, COL5A2, COL11A1, LUM, and inflammation-related genes like CXCL10 and CXCL12 were progressively upregulated. Further, the Geneswitch algorithm identified several biological processes activated across the pseudotime change from pCAF-mCAF-meCAF, including KRAS signaling, ECM, epithelial-mesenchymal transition, angiogenesis, and hypoxia (Figure S5A). Subsequent deconvolution analysis in the TCGA-OV cohort quantified the three states of CAFs during development and performed survival analysis (Figure S5B), showing that only state2, dominated by mCAF, significantly impacted survival, with higher expression of CAFs-state2 correlating with worse survival, while CAFs-state1 and CAFs-state3 had no statistically significant effect on survival.

In summary, during the differentiation and development of CAFs, pCAF represents the "initial state", mCAF the "transitional state", and meCAF the "terminal state". The "transitional state" mCAF affects the survival of OC patients possibly due to its ECM remodeling and inflammatory cytokine secretion functions, which influence the invasive capabilities of tumor cells via paracrine effects; whereas the "terminal state" meCAF might sustain tumor growth through metabolic reprogramming.

Cellular Communication in Tumor Microenviroment

In the OC ecosystem, cell-cell communication is extensive and complex.[38] Analysis using the CellChat algorithm revealed that endothelial and myeloid cells act as receivers with high input interaction intensity in both early and advanced-stage samples. However, in advanced-stage samples, the input and output interaction strengths of B cells, T cells, and NK cells are significantly reduced, likely due to the barrier effect of CAFs (Figure 6A). Compared to early-stage samples, tumor epithelial cells and CAFs in advanced-stage samples exhibit significantly increased output signal strength, while the input signal strength changes little. Compared to early-stage patients, advanced-stage patients show an increase in the number and intensity of actions by CAFs, while most immune cells show a decrease (Figure 6B).

Immune evasion is a key hallmark of cancer, and CAFs contribute to this process not only by providing a physical barrier but also by influencing the tumor microenvironment.[39] Our analysis focused on different states of CAFs, revealing specific

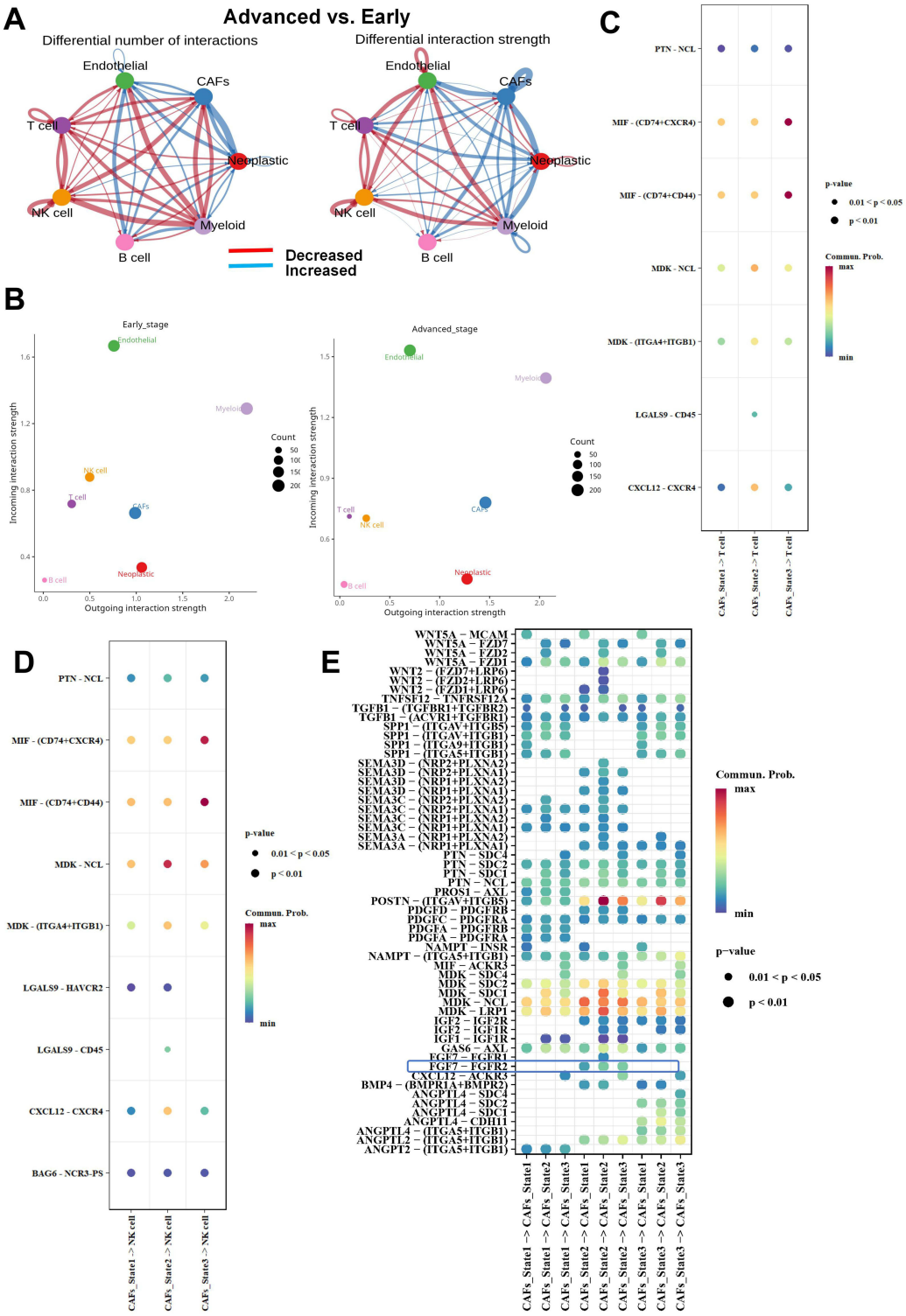

Figure 6 Cellular communication in the tumor microenvironment. (**A**) Network diagrams showing differential interactions among cell types in early-stage and advanced-stage ovarian cancer samples. The left diagram represents the differential number of interactions, and the right diagram represents the differential interaction strength. Red lines indicate decreased interactions, while blue lines indicate increased interactions. (**B**) Dot plots comparing incoming and outgoing interaction strengths of different cell types in early-stage (left) and advanced-stage (right) samples. The size of the dots represents the count of interactions. (**C**) Bubble plot showing key ligand-receptor pairs involved in cell-cell communication among CAFs, epithelial cells, endothelial cells, myeloid cells, NK cells, and T cells. The size of the bubbles indicates the common probability, and the color indicates the p-value significance. (**D**) Dot plots highlighting specific ligand-receptor pairs such as PTN-NCL, MIF-CD74+CXCR4, MIF-CD74 +CD44, MDK-NCL, MDK-ITGA4+ITGB1, LGALS9-HAVCR2, LGALS9-CD45, and CXCL12-CXCR4. The size and color of the dots represent the common probability and p-value significance. (**E**) Heatmap of significant ligand-receptor interactions among CAF subtypes (State 1, State 2, State 3) and other cell types. The color intensity represents the common probability, and the size of the dots indicates p-value significance.

https://doi.org/10.2147/JIR.S571158

communication patterns with NK/T cells shared across different CAF states. CAFs-state3 (dominated by meCAF) shows a higher likelihood of interaction with NK/T cells compared to CAF-state1 and CAF-state2, highlighting its potential immunomodulatory role (Figure 6C and D). Notably, the interaction potential with CD44,[40] crucial for T cell activation and navigation in anti-tumor immunity, is greatest with CAFs-state3, while LGALS9,[41] which regulates adaptive immunity, functions primarily in CAFs-state2.

Further analysis explored the cell communication between different CAF states and myeloid cells. Literature reports suggest that the CXCL12-CXCR3 interaction may recruit pDC cells, with CAFs-state2 showing the strongest cell communication potential. The interaction between LGALS9 and CD40 stimulates the activation and maturation of DC cells,[41] with similar functions observed in CAFs-state1 and CAFs-state2. However, overall, CAFs-state3 shows the strongest potential for cell communication, especially in the binding of the MIF ligand to other receptors (Figure S6A). Besides interactions with NK and T cells, CAFs may also regulate B cell maturation through overexpression of the MIF ligand interacting with CD74/CD44 on B cells, which play roles in B cell maturation and activation, with CAFs-state3 playing a dominant role (Figure S6B).

We also examined the crosstalk between different states of CAFs (Figure 6E), with all three states showing stronger cell communication potential via POSTN- (ITGAV+ITGB5). Importantly, the FGF7-FGFR1 ligand interaction might affect CAFs-state2 through autocrine signaling, while FGF7-FGFR2 could affect CAFs-state2 via autocrine signaling and CAFs-state3 and CAFs-state1 via paracrine signaling, stimulating a pan-CAF effect.

Additionally, we analyzed the primary communications with endothelial cells, essential for tumor angiogenesis. Interactions between endothelial cells and CAFs-state2/3 are more pronounced compared to CAFs-state1, including interactions such as MDK-NCL and MDK-ITAG6+ITGBI (Figure S6C). CAFs-state3 exclusively engages in interactions with VEGFA-VEGFR1R2, VEGFA-VEGFR1, and VEGFA-VEGFR2 ligands. Furthermore, the cell communication between the three CAF states and tumor epithelial cells was assessed (Figure S6D). Interestingly, CAFs-state2 shows more interactions with tumor epithelial cells than other states. Various CAF states demonstrate a high likelihood of communication through ligand-receptor pairs such as MDK-SDC1/2/4/NCL/LRP1/(ITGA6+ITGB1). CAFs-sate2, dominated by mCAF, uniquely engages in cell communication via the WNT2 ligand, such as WNT2-(FZD family+LRP family) receptor interaction. Meanwhile, CAFs-sate3, led by meCAF, exclusively engages in MIF-(CD74+CXCR4) receptor communication.

Spatial Distribution Characteristics of CAFs in Ovarian Cancer

To determine the spatial distribution characteristics of CAFs, we added annotation information of CAF subgroups to the CellTrek object. Density maps revealed spatial exclusivity between high-density areas of different CAF subgroups, suggesting that the activation states of CAFs may be related to their positions within the TME (Figure 7A). We calculated the spatial k-distance between other cell types and CAF subgroups in representative tissue sections, displayed using a heatmap. As expected, each type of CAF subtype was surrounded by other types of CAF subtypes. Compared to early-stage samples, the spatial distance between various cells and the three subtypes of CAF cells decreased in advanced-stage samples, indicating a potential increase in chemotactic effects due to the higher CAF content in these advanced-stage samples. Additionally, the Robust Rank Aggregation (RRA) is an algorithm that integrates ranks to generate a comprehensive ranking list. Cells were ranked from closest to furthest and integrated using the RRA algorithm to obtain a comprehensive ranking of all cells. The comparison of k-distances with mCAF showed that meCAF was the closest, followed by tumor epithelial cells and myeloid cells (Figure 7B and C). In comparisons with meCAF, mCAF was the closest, while there were no significant differences in distances to other cells (Figure 7D and E). Finally, in the distance comparison for pCAF, the top three closest were meCAF, mCAF, and myeloid cells (Figure 7F and G).

Overall, the spatial distribution characteristics of CAFs demonstrate that the three CAF subtypes are proximate to each other, with mCAF being closest to tumor cells, possibly facilitating the strongest spatial communication.

Characterization of Key Genes of CAFs

In our previous research, we found that the CAF-derived FGF7 can promote malignant behavior by activating the FGF and EMT signaling pathways in tumor cells.[38] Quantitative analysis of CAF subtypes showed a stepwise expression pattern of FGF7, with the lowest expression in pCAF, higher in meCAF, and the highest in mCAF (Figure S7A). Considering the paracrine action of FGF7 on FGFR2 receptors on tumor epithelial cells and the autocrine action on FGFR2 receptors on

 https://doi.org/10.2147/JIR.S571158

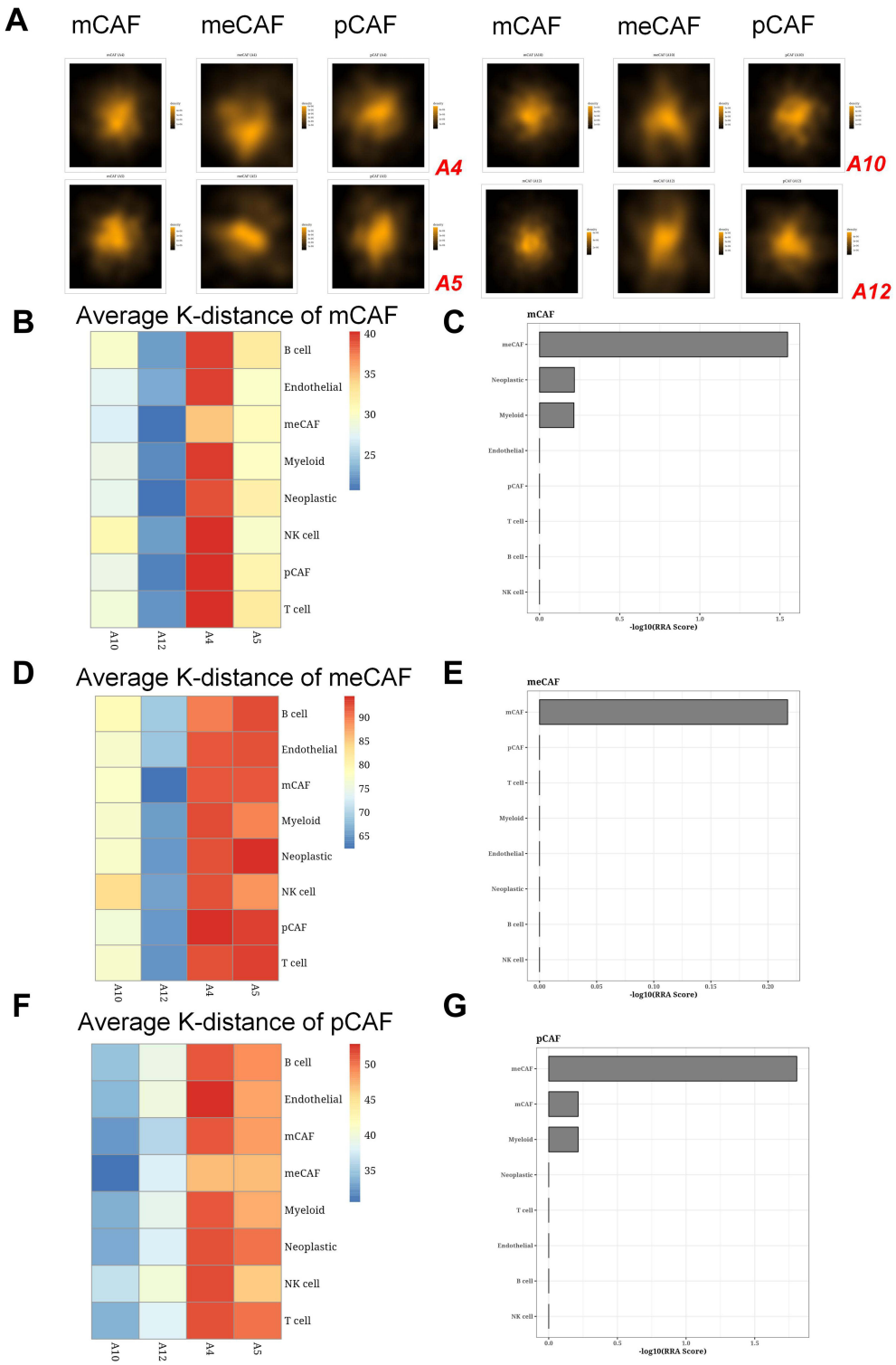

Figure 7 Spatial distribution and interaction analysis of CAFs in ovarian cancer. (**A**) Density maps showing the spatial distribution of different cell types (B cells, endothelial cells, mCAFs, myeloid cells, neoplastic cells, NK cells, pCAFs, and T cells) in early-stage samples (A4, A5) and advanced-stage samples (A10, A12). The intensity of the color represents the density of each cell type. (**B**) Heatmap comparing the interaction strengths among various cell types in early-stage samples, with colors indicating interaction strength. (**C**) Bar plot of the top interaction pairs involving mCAFs in early-stage samples. The x-axis represents the log-transformed interaction strength. (**D**) Heatmap comparing the interaction strengths among various cell types in advanced-stage samples, with colors indicating interaction strength. (**E**) Bar plot of the top interaction pairs involving meCAFs in advanced-stage samples. The x-axis represents the log-transformed interaction strength. (**F**) Heatmap comparing the interaction strengths among various cell types in early-stage samples, with colors indicating interaction strength. (**G**) Bar plot of the top interaction pairs involving pCAFs in early-stage samples. The x-axis represents the log-transformed interaction strength.

https://doi.org/10.2147/JIR.S571158

various CAF subtypes, which broadly activates CAFs, we conducted a detailed analysis of the FGF7-FGFR2 axis. Differential analysis among various cell types revealed that FGF7 is predominantly expressed in CAFs (Figure S7B), while FGFR2 is primarily expressed in both CAFs and tumor epithelial cells (Figure S7C). Grouping by tumor stage showed significant upregulation of both FGF7 and FGFR2 in late-stage samples (Figure S7D and E). Using the AddModuleScore algorithm to calculate ligand-receptor co-expression intensity in spatial transcriptomics data, we observed increased expression density of FGF7/FGFR2 in late-stage samples A10 and A12 (Figure S7F). In summary, we propose that this ligand-receptor interaction plays a critical role in tumor progression and the functional maintenance of CAFs.

We hypothesize that the autocrine action of FGF7 may play a critical role in the sustained activation of CAFs. Activated CAFs can enhance the contraction of the ECM, increasing its rigidity and density, thereby influencing the physical properties of the tumor microenvironment.[42] Using the ESTIMATE algorithm to analyze the stromal scores in different datasets (Figure S7G), we found a significant positive correlation between FGF7 expression and stromal scores ($r > 0.3$, $P < 0.05$). Furthermore, α-SMA (ACTA2) is an important marker for evaluating CAF activation, with increased expression reflecting cytoskeletal reorganization and enhanced contractility during CAF activation. In the microdissected datasets, a significant positive correlation was observed between the expression levels of FGF7 and ACTA2 in the tumor stroma ($r = 0.579$, $P < 0.05$) (Figure S7H).

FGF7 Activates the PI3K-AKT Pathway to Maintain CAF Activation

TGF-β is a crucial multifunctional cytokine in the tumor microenvironment.[43] Fibroblasts exposed to TGF-β express CAF markers and acquire CAF characteristics, including enhanced migratory and contractile abilities and ECM remodeling, through the activation of the Smad signaling pathway.[44,45] MRC5 cells were used to create CAF-like cells (MRC5-CAFs) as a supplementary control for primary fibroblasts.[11] Western blot results showed that MRC5 cells exhibited a CAF phenotype after TGF-β stimulation (Figure 8A). RNA-seq analysis of MRC5-CAFs and MRC5 revealed that when MRC5 cells transitioned to a CAF-like phenotype, the mRNA levels of several ECM-related genes, including ACTA2, ITAG9, and IGFL3, were significantly elevated (Figure 8B). Pathway enrichment analysis based on differentially expressed genes showed that the PI3K-AKT pathway was the top-ranked pathway (Figure 8C). A collagen contraction assay further confirmed that the contractile ability of both CAFs and MRC5-CAFs increased with higher FGF7 concentrations (Figure 8D). However, neutralizing FGF7 in the medium or using an FGFR2 antagonist reduced the contractile ability of CAFs (Figure 8E). These findings indicate that CAF-derived FGF7 significantly impacts their activation state. Subsequent Western blot analysis validated changes in the protein levels of α-SMA, AKT, and p-AKT in CAFs under different conditions: stimulation with various concentrations of hFGF7, addition of an FGF7 neutralizing antibody, and FGFR2 antagonist. The results demonstrated that with increasing FGF7 concentrations, α-SMA expression increased, AKT protein levels remained constant, and p-AKT protein levels rose, indicating that the PI3K-AKT pathway was activated by hFGF7 stimulation (Figure 8F). Conversely, neutralizing FGF7 in the medium and inhibiting FGFR2 significantly reduced the expression of the CAF activation marker α-SMA and the p-AKT protein level, indicating inhibition of the PI3K-AKT pathway (Figure 8G).

These findings suggest that CAFs may maintain their activation state through the FGF7/FGFR2-mediated activation of the PI3K-AKT pathway.

Discussion

Our study are consistent with previous research, identifying multiple cell types (including epithelial cells, CAFs, T cells, B cells, NK cells, myeloid cells, and endothelial cells), revealing significant intratumoral heterogeneity in OC.[46] In contrast to other studies, we found relatively low heterogeneity in the stromal area when dividing the tumor region and the non-tumor region, with representative subgroups of stroma in different stages. Representative genes in late-stage stromal subgroups, such as SPP1 and LDHA, are usually associated with the invasiveness and energy metabolism regulation of tumor cells. In early-stage samples, CLU and BCYRN1, as key markers, are related to cell cycle and apoptosis regulation. Due to the low heterogeneity in the tumor stroma, targeting the stroma may be key to addressing varying treatment responses in patients with the same stage and pathology.

CAFs demonstrate significant plasticity and heterogeneity, identified in ascites and tumor tissues of OC. Hussain et al[47] described four CAF subgroups (CAF-S1–S4) in HGSOC and suggested that the accumulation of CAF-S1 is associated with an

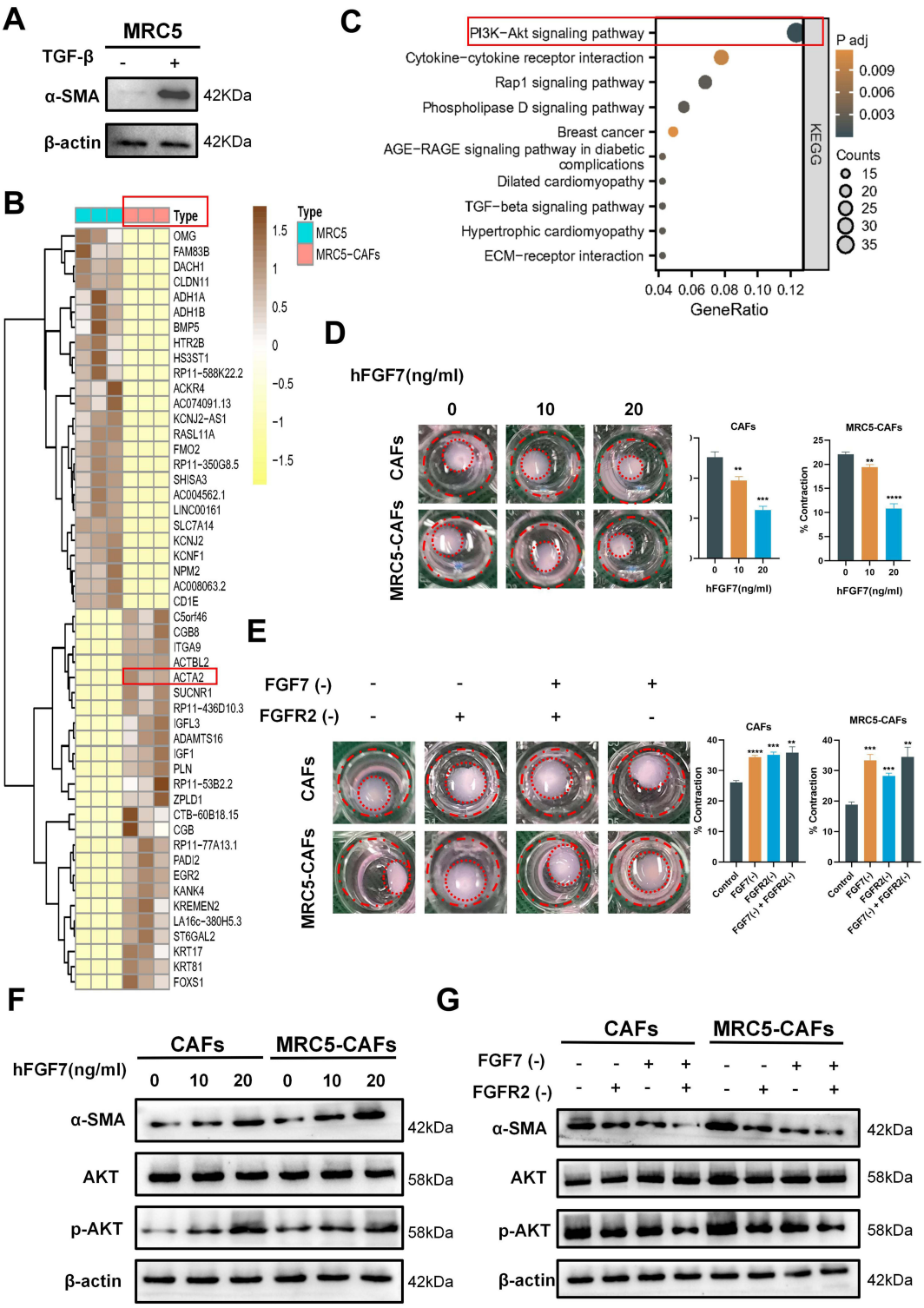

Figure 8 FGF7 activates the PI3K-AKT pathway to maintain CAF activation. (**A**) Western blot analysis showing the expression of CAF markers in MRC5 cells after TGF-β stimulation, confirming the CAF phenotype. (**B**) Heatmap displaying the RNA-seq results for MRC5-CAFs and MRC5 cells, indicating significant elevation of ECM-related genes, including ACTA2, in the CAF-like phenotype. (**C**) KEGG pathway enrichment analysis based on differentially expressed genes, highlighting the PI3K-AKT signaling pathway as the top enriched pathway. (**D**) Collagen contraction assay results showing increased contractile ability of CAFs and MRC5-CAFs with higher hFGF7 concentrations. Bar graphs quantify the percentage contraction for each condition. (**E**) Collagen contraction assay results showing the reduction in contractile ability with FGF7 neutralization or FGFR2 antagonism in CAFs and MRC5-CAFs. Bar graphs quantify the percentage contraction for each condition. (**F**) Western blot analysis validating changes in α-SMA, AKT, and p-AKT protein levels in CAFs under various concentrations of hFGF7, addition of FGF7 neutralizing antibody, and FGFR2 antagonist. (**G**) Western blot analysis validating changes in α-SMA, AKT, and p-AKT protein levels in CAFs under addition of FGF7 neutralizing antibody, and FGFR2 antagonist. Data are presented as mean ± SEM (n=3 per group). **P < 0.01, ***P < 0.001, ****P < 0.0001.

https://doi.org/10.2147/JIR.S571158

immunosuppressive tumor environment. Izar et al identified four CAF subgroups, two of which express immune-related genes.[3] Carvalho et al proposed that iCAF1 is associated with genes related to hypoxia and TNF-α signaling via NF-KB, while iCAF2 is highly correlated with oxidative phosphorylation.[46] In our study, CAFs in OC were classified into three subtypes based on function and secretion characteristics: mCAF, meCAF, and pCAF. Among them, mCAF exhibits inflammatory response and chemokine secretion functions similar to iCAF in pan-cancer analysis. Unlike previous studies, we defined three developmental states of CAFs for subsequent analysis through cell developmental trajectories: state 1 (dominated by pCAF), state 2 (dominated by mCAF), and state 3 (dominated by meCAF). This approach minimizes classification sensitivity issues caused by different resolutions when reducing subgroups.

Previous studies have investigated the similarities of CAFs between different cancer types. The pan-myCAF is associated with high expression of genes related to angiogenesis and ECM remodeling.[48] Furthermore, some studies suggest that antigen-presenting CAFs (apCAF) subtype expresses major histocompatibility complex class II genes,[49] described only in mouse and human pancreatic cancer, lung cancer, breast cancer, and cholangiocarcinoma. However, in our study, we did not identify the presence of myCAF and apCAF, and the function of myCAF is similar to our mCAF function. Indeed, one of the challenges facing the scientific community is reaching a consensus on the classification and naming of CAFs. Therefore, due to the inconsistency in CAFs classification, we discuss their functional characteristics from a broader perspective, focusing on the functional properties of CAFs rather than specific subtype names.

In the process of CAFs differentiation and development, pCAF is the "initial state", mCAF is the "transitional state", and meCAF is the "terminal state". During the development process towards state 3 (dominated by meCAF), the expression of metabolic genes such as ANGPTL4, SLC2A1, and PGK1 increases, while cytokine-related genes such as CXCL10, CXCL12, ECM-related genes such as COL3A1, and COL1A1 decrease. Unlike state 3, in the development process towards state 2 (dominated by mCAF), the expression of ECM-related genes and inflammation-related genes gradually increases over time. In the analysis of CAFs heterogeneity, we identified the mCAF subtype as the main subtype involved in ECM remodeling. ZEB1 transcription factor plays a leading role in mCAF, indicating that the conversion of this highly invasive CAFs phenotype may require EMT. We found that in the TCGA cohort, only state 2 dominated by mCAF has a statistically significant impact on survival, where higher expression of CAFs-state 2 is associated with poorer survival. Similarly, in the pan-cancer analysis of CAFs, mCAF is associated with poor prognosis in gastric cancer and produces collagen to provide a physical barrier, impairing the transport of adaptive immune cells to new antigen presentation sites.[9] Additionally, in spatial analysis, we found that mCAF closest to the tumor area highly expresses collagen genes, further supporting the hypothesis that specific CAFs produce a physical barrier by generating dense ECM to prevent immune cells from entering the tumor area.

Furthermore, we identified the pCAF subtype as the main subtype involved in cell proliferation and lineage development. pCAF consists mainly of subgroups 4, 5, 7, and 8 in the CAFs clustering classification, with GO analysis enriched in processes such as ribonucleoprotein complex biogenesis. Ribosome biogenesis is a tightly regulated multi-step process involving the synthesis and processing of ribosomal RNA, production of ribosomal proteins, and subsequent assembly and maturation of ribosomes.[50] It has been confirmed that disruption of any single step in ribosome biogenesis, such as by antibiotics like actinomycin D or CX-5461, induces severe cytotoxic effects, known as ribosomal or nucleolar stress, releasing tumor suppressive signals involving activation of tumor suppressors p53 and TAp73 and inhibition of the c-Myc pathway.[51–53] Inhibiting ribosome biogenesis may be crucial for inhibiting the initiation of pCAF, the source of CAFs differentiation and development.

We identified a subtype that maintains tumor growth mainly through metabolic reprogramming and hypoxia response at the differentiation end: meCAF. Glycolysis and amino acid metabolism pathways are significantly enriched in meCAF, suggesting that CAFs provide energy to cancer cells through glycolysis in the hypoxic tumor microenvironment, possibly induced by the reverse Warburg effect caused by meCAF. In pancreatic cancer, the presence of meCAF has also been found, suggesting that abundant meCAFs produce a large amount of catabolic metabolism fuel to support mitochondrial OXPHOS activity in cancer cells, thus promoting tumor progression.[23] Therefore, understanding the developmental trajectory and characteristics of meCAF and developing targeted therapies may improve the treatment efficacy of OC and other cancers.

Gene regulatory networks are manifested through the regulation of numerous transcription factors and their downstream target genes, forming the molecular basis of cellular states. We performed SCENIC analysis on CAFs. In mCAFs, the top four transcription factors are FOS, FOSL2, JUN, and JUND; in pCAFs, they are MEF2C, FOS, JUN, and JUND; in meCAFs, they

are FOSL1, CEBPB, DDIT3, and GLIS2. pCAFs and mCAFs share similar transcriptional activation (FOS, JUN, JUND), whereas meCAFs exhibit significant changes, with only the FOSL family being consistent. This suggests that pCAFs and mCAFs are developmentally closer, while meCAFs are more differentiated. Clinically significant, recent studies have demonstrated that inhibiting JUN with the JUN/AP-1 inhibitor T-5224, used for inflammatory diseases, can markedly inhibit the growth and migration of OC cells, providing initial evidence of JUN as a potential therapeutic target for OC.[54]

Increasing evidence indicates that the communication and interaction between cancer cells and CAFs are crucial determinants of tumor metastasis and progression. Interestingly, CAFs-state2 exhibited more interactions with tumor epithelial cells than other states. CAFs-state2, dominated by mCAFs, uniquely featured WNT2 ligand-cell communication, such as WNT2-(FZD family + LRP family) receptor-ligand interactions. In contrast, CAFs-state3, dominated by meCAFs, featured unique MIF-(CD74 + CXCR4) receptor-ligand communication.

We created a CAF-like cell line (MRC5-CAFs) using the MRC5 cell line as a supplemental control for primary fibroblasts and performed RNA-seq analysis on both MRC5-CAFs and MRC5 cells. The results showed that the PI3K-AKT pathway was the most enriched pathway when MRC5 cells transitioned to a CAF-like phenotype. Experimental validation involved stimulating CAFs with various concentrations of hFGF7 and adding an FGF7 neutralizing antibody and an FGFR2 antagonist. We observed changes in the levels of α-SMA, AKT, and p-AKT proteins, as well as ECM contraction ability in CAFs. The results suggest that stromal CAFs may maintain their activated state through the FGF7/FGFR2 activation of the PI3K-AKT pathway. Currently, there is limited research on how CAFs maintain activation through the PI3K-AKT pathway, but it is well-established that this pathway is linked to fibroblast activity, particularly in fibrosis and keloid formation. A study on fibroblasts derived from Peyronie's plaques found that inhibiting the PI3K-AKT pathway with a novel inhibitor, HS-173, resulted in dose-dependent growth inhibition and apoptosis induction in fibroblasts.[55] Furthermore, HS-173 reduced α-SMA expression, indicating its potential antifibrotic effects. Inhibition of this pathway can alter the glucose metabolism of keloid fibroblasts; under hypoxic conditions, inhibiting the PI3K-AKT pathway in fibroblasts reduces glycolytic enzyme levels, glucose uptake, and weakens the Warburg effect.[56]

Our study has several notable limitations. First, our work is omics-based, necessitating validation of the different CAF subtypes through experimental methods such as fluorescence-activated cell sorting and immunohistochemistry. Second, despite our efforts to ensure robust CAF clustering analysis, the clustering results can be further refined and improved with larger datasets and updated bioinformatics algorithms. Third, in our TCGA survival analysis, we relied on ssGSEA to assess the prognostic role of individual CAF subtypes. While this enhances clinical relevance, the results could be improved using other methods to determine cell population abundance.

Overall, this study comprehensively characterizes three common CAF subtypes in OC samples from the Chinese population and suggests that OC may benefit from subtype-specific CAF-targeted therapies.

Conclusion

The tumor microenvironment in OC patients is highly heterogeneous, particularly within the tumor region, while the stroma region shows weaker heterogeneity and can serve as an effective therapeutic target. The OC microenvironment is highly immunosuppressive, with dense CAFs preventing immune cells from infiltrating the tumor interior. This results in a "cold environment" in both early and late-stage patients. CAFs in OC can be categorized into three subtypes: mCAF, meCAF, and pCAF. pCAF is the "initial state", mCAF is the "transitional state", and meCAF is the "terminal state". The mCAF subtype affects patient survival the most due to its ECM remodeling and inflammatory cytokine secretion, which enhance tumor cell invasiveness through paracrine signaling. meCAF supports tumor growth through metabolic reprogramming, while pCAF exhibits the strongest proliferation and differentiation capabilities. More importantly, autocrine FGF7 from CAFs can act on their own FGFR2, activating the PI3K-AKT pathway and contributing to the maintenance of ECM contraction by CAFs.

Data Sharing Statement

The following information was supplied regarding data availability: data is available at the TCGA (https://portal.gdc.cancer.gov/), GEO database (https://www.ncbi.nlm.nih.gov/geo/), and codeocean database (https://codeocean.com/). The detailed data that support the findings of this study are available from the corresponding author upon reasonable request.

Ethics Approval and Consent to Participate

The studies involving human participants were reviewed and approved by the Ethics Committees and Institutional Review Boards of Zhongda Hospital Southeast University (ZDSYLL187-P04). All procedures performed in this study involving human participants were in accordance with the ethical standards of the Declaration of Helsinki.

Acknowledgments

We are grateful to the staff in Biobank of Zhongda Hospital Affiliated to Southeast University for technical assistance.

Author Contributions

Songwei Feng: Conceptualization, Methodology, Investigation, Writing – Original Draft. Zhaoyan Ding: Data Curation, Writing – Original Draft. Yuru Wang: Investigation, Formal analysis, Writing – Original Draft. Zihan Zhu: Validation, Writing – Original Draft. Wen Zhong: Software, Writing – Original Draft. Ke Zhang: Conceptualization, Supervision, Writing – Review & Editing. Yueming Zhang: Methodology, Project administration, Supervision, Writing – Review & Editing. Li Chen: Supervision, Writing – Original Draft, Writing – Review & Editing. Yun Ma: Funding acquisition, Resources, Project administration, Writing – Review & Editing. All authors gave final approval of the version to be published; have agreed on the journal to which the article has been submitted; and agree to be accountable for all aspects of the work.

Funding

This work was supported by the National Natural Science Foundation of China (No. 82503307), Postdoctoral Fellowship Program of CPSF (No. GZC20251352), the China Postdoctoral Science Foundation (No. 2024M762304), and the Suzhou Medical College-QiLu Medical Research Program of Soochow University (No. 24QL200112).

Disclosure

There are no conflicts of interest regarding the publication of this article.

References

1. Stokes T, Cen HH, Kapranov P, et al. Transcriptomics for clinical and experimental biology research: Hang on a Seq. *Adv Genet*. 2023;4(2):2200024. doi:10.1002/ggn2.202200024
2. Chen G, Xu W, Long Z, et al. Single-cell technologies provide novel insights into liver physiology and pathology. *J Clin Transl Hepatol*. 2024;12(1):79–90. doi:10.14218/JCTH.2023.00224
3. Izar B, Tirosh I, Stover EH, et al. A single-cell landscape of high-grade serous ovarian cancer. *Nat Med*. 2020;26(8):1271–1279. doi:10.1038/s41591-020-0926-0
4. Zhang M, Chen Z, Wang Y, et al. The role of cancer-associated fibroblasts in ovarian cancer. *Cancers*. 2022;14(11).
5. Chen Y, Mcandrews KM, Kalluri R. Clinical and therapeutic relevance of cancer-associated fibroblasts. *Nat Rev Clin Oncol*. 2021;18(12):792–804. doi:10.1038/s41571-021-00546-5
6. Givel AM, Kieffer Y, Scholer-Dahirel A, et al. miR200-regulated CXCL12beta promotes fibroblast heterogeneity and immunosuppression in ovarian cancers. *Nat Commun*. 2018;9(1):1056. doi:10.1038/s41467-018-03348-z
7. Galbo PM, Zang X, Zheng D. Molecular features of cancer-associated fibroblast subtypes and their implication on cancer pathogenesis, prognosis, and immunotherapy resistance. *Clin Cancer Res*. 2021;27(9):2636–2647. doi:10.1158/1078-0432.CCR-20-4226
8. Luo H, Xia X, Huang LB, et al. Pan-cancer single-cell analysis reveals the heterogeneity and plasticity of cancer-associated fibroblasts in the tumor microenvironment. *Nat Commun*. 2022;13(1):6619. doi:10.1038/s41467-022-34395-2
9. Ma C, Yang C, Peng A, et al. Pan-cancer spatially resolved single-cell analysis reveals the crosstalk between cancer-associated fibroblasts and tumor microenvironment. *Mol Cancer*. 2023;22(1):170. doi:10.1186/s12943-023-01876-x
10. Abuwarwar MH, Baker AT, Harding J, et al. In vitro suppression of T cell proliferation is a conserved function of primary and immortalized human cancer-associated fibroblasts. *Int J Mol Sci*. 2021;22(4):1827. doi:10.3390/ijms22041827
11. Li X, Fang T, Xu S, et al. PARP inhibitors promote stromal fibroblast activation by enhancing CCL5 autocrine signaling in ovarian cancer. *NPJ Precis Oncol*. 2021;5(1):49. doi:10.1038/s41698-021-00189-w
12. Liu Z, Liu J, Chen T, et al. Wnt-TCF7-SOX9 axis promotes cholangiocarcinoma proliferation and pemigatinib resistance in a FGF7-FGFR2 autocrine pathway. *Oncogene*. 2022;41(20):2885–2896. doi:10.1038/s41388-022-02313-x
13. Zhang J, Wong CC, Leung KT, et al. FGF18-FGFR2 signaling triggers the activation of c-Jun-YAP1 axis to promote carcinogenesis in a subgroup of gastric cancer patients and indicates translational potential. *Oncogene*. 2020;39(43):6647–6663. doi:10.1038/s41388-020-01458-x
14. Magrill J, Moldoveanu D, Gu J, et al. Mapping the single cell spatial immune landscapes of the melanoma microenvironment. *Clin Exp Metastasis*. 2024;41:301–312. doi:10.1007/s10585-023-10252-4
15. Xiao Z, Dai Z, Locasale JW. Metabolic landscape of the tumor microenvironment at single cell resolution. *Nat Commun*. 2019;10(1):3763.

16. Robles-Remacho A, Sanchez-Martin RM, Diaz-Mochon JJ. Spatial transcriptomics: emerging technologies in tissue gene expression profiling. *Anal Chem*. 2023;95(42):15450–15460.
17. Aibar S, Gonzalez-Blas CB, Moerman T, et al. SCENIC: single-cell regulatory network inference and clustering. *Nat Methods*. 2017;14(11):1083–1086. doi:10.1038/nmeth.4463
18. Bibby JA, Agarwal D, Freiwald T, et al. Systematic single-cell pathway analysis to characterize early T cell activation. *Cell Rep*. 2022;41(8):111697. doi:10.1016/j.celrep.2022.111697
19. Chen X, Ye Z, Lou P, et al. Comprehensive analysis of metabolism-related lncRNAs related to the progression and prognosis in osteosarcoma from TCGA. *J Orthop Surg Res*. 2021;16(1):523. doi:10.1186/s13018-021-02647-4
20. Street K, Risso D, Fletcher RB, et al. Slingshot: cell lineage and pseudotime inference for single-cell transcriptomics. *BMC Genomics*. 2018;19(1):477. doi:10.1186/s12864-018-4772-0
21. Cao EY, Ouyang JF, Rackham OJL. GeneSwitches: ordering gene expression and functional events in single-cell experiments. *Bioinformatics*. 2020;36(10):3273–3275. doi:10.1093/bioinformatics/btaa099
22. Jin S, Guerrero-Juarez CF, Zhang L, et al. Inference and analysis of cell-cell communication using CellChat. *Nat Commun*. 2021;12(1):1088.
23. Wang Y, Liang Y, Xu H, et al. Single-cell analysis of pancreatic ductal adenocarcinoma identifies a novel fibroblast subtype associated with poor prognosis but better immunotherapy response. *Cell Discov*. 2021;7(1):36.
24. Liu C, Zhang M, Yan X, et al. Single-cell dissection of cellular and molecular features underlying human cervical squamous cell carcinoma initiation and progression. *Sci Adv*. 2023;9(4):eadd8977. doi:10.1126/sciadv.add8977
25. Yu Z, Zhu J, Wang H, et al. Function of BCLAF1 in human disease. *Oncol Lett*. 2022;23(2):58. doi:10.3892/ol.2021.13176
26. Scheurlen KM, Chariker JH, Kanaan Z, et al. The NOTCH4-GATA4-IRG1 axis as a novel target in early-onset colorectal cancer. *Cytokine Growth Factor Rev*. 2022;67:25–34. doi:10.1016/j.cytogfr.2022.06.002
27. Fang Z, Lin M, Li C, et al. A comprehensive review of the roles of E2F1 in colon cancer. *Am J Cancer Res*. 2020;10(3):757–768.
28. Saito A, Omura I, Imaizumi K. CREB3L1/OASIS: cell cycle regulator and tumor suppressor. *FEBS J*. 2024;291:4853–4866. doi:10.1111/febs.17052
29. Zhu J, Huang Z, Zhang M, et al. HIF-1alpha promotes ZEB1 expression and EMT in a human bladder cancer lung metastasis animal model. *Oncol Lett*. 2018;15(3):3482–3489. doi:10.3892/ol.2018.7764
30. Feng H, Zhang YB, Gui JF, et al. Interferon regulatory factor 1 (IRF1) and anti-pathogen innate immune responses. *PLoS Pathog*. 2021;17(1):e1009220. doi:10.1371/journal.ppat.1009220
31. Ku HC, Cheng CF. Master regulator Activating Transcription Factor 3 (ATF3) in metabolic homeostasis and cancer. *Front Endocrinol*. 2020;11:556. doi:10.3389/fendo.2020.00556
32. Wang XL, Li J, Cao YH. Crosstalk between YY1 and lncRNAs in cancer: a review. *Medicine*. 2022;101(49):e31990. doi:10.1097/MD.0000000000031990
33. Chen S, Chen J, Hua X, et al. The emerging role of XBP1 in cancer. *Biomed Pharmacother*. 2020;127:110069. doi:10.1016/j.biopha.2020.110069
34. Song D, Lian Y, Zhang L. The potential of activator protein 1 (AP-1) in cancer targeted therapy. *Front Immunol*. 2023;14:1224892. doi:10.3389/fimmu.2023.1224892
35. Fernandez-Hernando C, Suarez Y. ANGPTL4: a multifunctional protein involved in metabolism and vascular homeostasis. *Curr Opin Hematol*. 2020;27(3):206–213. doi:10.1097/MOH.0000000000000580
36. He Y, Luo Y, Zhang D, et al. PGK1-mediated cancer progression and drug resistance. *Am J Cancer Res*. 2019;9(11):2280–2302.
37. Sharma D, Singh M, Rani R. Role of LDH in tumor glycolysis: regulation of LDHA by small molecules for cancer therapeutics. *Semin Cancer Biol*. 2022;87:184–195. doi:10.1016/j.semcancer.2022.11.007
38. Feng S, Ding B, Dai Z, et al. Cancer-associated fibroblast-secreted FGF7 as an ovarian cancer progression promoter. *J Transl Med*. 2024;22(1):280. doi:10.1186/s12967-024-05085-y
39. Jhunjhunwala S, Hammer C, Delamarre L. Antigen presentation in cancer: insights into tumour immunogenicity and immune evasion. *Nat Rev Cancer*. 2021;21(5):298–312. doi:10.1038/s41568-021-00339-z
40. Hassn Mesrati M, Syafruddin SE, Mohtar MA, et al. CD44: a Multifunctional Mediator of Cancer Progression. *Biomolecules*. 2021;11(12):1850. doi:10.3390/biom11121850
41. Lv Y, Ma X, Ma Y, et al. A new emerging target in cancer immunotherapy: galectin-9 (LGALS9). *Genes Dis*. 2023;10(6):2366–2382. doi:10.1016/j.gendis.2022.05.020
42. Feng X, Liu X, Xiang J, et al. Exosomal ITGB6 from dormant lung adenocarcinoma cells activates cancer-associated fibroblasts by KLF10 positive feedback loop and the TGF-beta pathway. *Transl Lung Cancer Res*. 2023;12(12):2520–2537. doi:10.21037/tlcr-23-707
43. Yeung TL, Leung CS, Wong KK, et al. TGF-beta modulates ovarian cancer invasion by upregulating CAF-derived versican in the tumor microenvironment. *Cancer Res*. 2013;73(16):5016–5028. doi:10.1158/0008-5472.CAN-13-0023
44. Wang QR, Liu SS, Min JL, et al. CCL17 drives fibroblast activation in the progression of pulmonary fibrosis by enhancing the TGF-beta/Smad signaling. *Biochem Pharmacol*. 2023;210:115475. doi:10.1016/j.bcp.2023.115475
45. Yang N, Hellevik T, Berzaghi R, et al. Radiation-induced effects on TGF-beta and PDGF receptor signaling in cancer-associated fibroblasts. *Cancer Rep*. 2024;7(3):e2018.
46. Carvalho RF, Do Canto LM, Abildgaard C, et al. Single-cell and bulk RNA sequencing reveal ligands and receptors associated with worse overall survival in serous ovarian cancer. *Cell Commun Signal*. 2022;20(1):176. doi:10.1186/s12964-022-00991-4
47. Hussain A, Voisin V, Poon S, et al. Distinct fibroblast functional states drive clinical outcomes in ovarian cancer and are regulated by TCF21. *J Exp Med*. 2020;217(8). doi:10.1084/jem.20191094
48. Brechbuhl HM, Finlay-Schultz J, Yamamoto TM, et al. Fibroblast subtypes regulate responsiveness of luminal breast cancer to estrogen. *Clin Cancer Res*. 2017;23(7):1710–1721. doi:10.1158/1078-0432.CCR-15-2851
49. Macy AM, Herrmann LM, Adams AC, et al. Major histocompatibility complex class II in the tumor microenvironment: functions of nonprofessional antigen-presenting cells. *Curr Opin Immunol*. 2023;83:102330. doi:10.1016/j.coi.2023.102330
50. Fatica A, Tollervey D. Making ribosomes. *Curr Opin Cell Biol*. 2002;14(3):313–318. doi:10.1016/S0955-0674(02)00336-8
51. Zhou X, Liao WJ, Liao JM, et al. Ribosomal proteins: functions beyond the ribosome. *J Mol Cell Biol*. 2015;7(2):92–104. doi:10.1093/jmcb/mjv014

52. Zhou X, Hao Q, Liao JM, et al. Ribosomal protein S14 negatively regulates c-Myc activity. *J Biol Chem*. 2013;288(30):21793–21801. doi:10.1074/jbc.M112.445122
53. Dai MS, Arnold H, Sun XX, et al. Inhibition of c-Myc activity by ribosomal protein L11. *EMBO J*. 2007;26(14):3332–3345. doi:10.1038/sj.emboj.7601776
54. Hao Q, Li J, Zhang Q, et al. Single-cell transcriptomes reveal heterogeneity of high-grade serous ovarian carcinoma. *Clin Transl Med*. 2021;11(8):e500. doi:10.1002/ctm2.500
55. Jung KH, Ryu YL, Lee HS, et al. A novel PI3K inhibitor alleviates fibrotic responses in fibroblasts derived from Peyronie's plaques. *Int J Oncol*. 2013;42(6):2001–2008. doi:10.3892/ijo.2013.1905
56. Wang Q, Yang X, Ma J, et al. PI3K/AKT pathway promotes keloid fibroblasts proliferation by enhancing glycolysis under hypoxia. *Wound Repair Regen*. 2023;31(2):139–155. doi:10.1111/wrr.13067